

Probable evidence for a transient mega-electron volt emission line in the GRB 221023A

Received: 23 October 2024

Accepted: 28 February 2025

Published online: 18 March 2025

Lu-Yao Jiang^{1,2}, Yun Wang¹, Yu-Jia Wei^{1,2,3,4}, Da-Ming Wei^{1,2}✉, Xiang Li^{1,2}, Hao-Ning He^{1,2}, Jia Ren¹, Zhao-Qiang Shen¹ & Zhi-Ping Jin^{1,2}

Detection of spectral line in gamma-ray bursts (GRBs) is importance for studying GRB physics, as it provides insights into the composition and physical conditions of the GRB environment. However, progress in detecting X-ray or gamma-ray emission and absorption lines in GRB spectra has been relatively slow, only the narrow emission line feature of about 10 MeV found in GRB 221009A has exhibited a significance exceeding 5σ . Here, we report the probable evidence of a narrow emission feature at about 2.1 mega-electron volts (MeV) in the spectrum of GRB 221023A. The highest statistical significance of this feature is observed in the time interval between 8 and 30 seconds after Fermi Gamma-Ray Burst Monitor trigger, with the chance probability value $<2.56 \times 10^{-5}$ (after accounting for the look-elsewhere effect), corresponding to a Gaussian-equivalent significance $>4.20\sigma$. We interpret this feature as being generated through the de-excitation of excited electrons in the relativistic hydrogen-like high-atomic-number ions entrained in the GRB jet.

Gamma-ray bursts (GRBs) are the most luminous stellar explosions in the universe. These events generally appear as brief and intense γ -rays followed by a long-lived afterglow emission. The GRB prompt emission originates from relativistic jets that dissipate the energy and accelerate particles either via internal shocks or magnetic reconnection, with high variability and usually lasts from milliseconds to thousands of seconds^{1–3}. Most of the observed spectrum of GRB prompt emission in the keV to MeV energy range usually can be described by a smoothly joint broken power-law function (called the Band function⁴). Despite decades of intensive investigation, our understanding of the physics behind the prompt emission of GRBs remains limited.

The existence of X-ray or gamma-ray emission and absorption lines in the GRB energy spectrum has been debated. For example, in prompt emission phase, the Konus instrument detected absorption lines at 30–70 keV and emission lines at 400–460 keV in the energy

spectra of some GRBs^{5,6}. HEAO-1 observed absorption-like features in the spectra of some GRBs^{7,8}. The Japanese Ginga Gamma-Ray Burst Detector (GBD) observed two absorption-like features in three GRBs (GRB 870303, GRB 880205 and GRB 890929), which may be interpreted as the first and second cyclotron absorption lines^{9–11}. Additionally, some 6.4 keV iron K- α spectral lines were claimed to have been found in some bursts. Within the energy range of 3.8 ± 0.3 keV, a possible transient Fe absorption feature was identified in the prompt X-ray spectrum of GRB 990705. This feature appeared during the initial rising phase of the burst profile and disappeared thereafter¹². In another study, Frontera et al.¹³ analyzed the prompt emission spectrum of GRB 011211 and found potential indications of transient Fe absorption features around 6.9 ± 0.6 keV during the rise of the main pulse. However, the statistical significance of these features is found to be below the 5σ threshold. Even when extending the spectral lines

¹Key Laboratory of Dark Matter and Space Astronomy, Purple Mountain Observatory, Chinese Academy of Sciences, Nanjing 210023, China. ²School of Astronomy and Space Science, University of Science and Technology of China, Hefei 230026, China. ³Department of Astronomy and Astrophysics, The Pennsylvania State University, 525 Davey Laboratory, University Park, PA 16802, USA. ⁴Institute for Gravitation and the Cosmos, The Pennsylvania State University, University Park, PA 16802, USA. ✉e-mail: dmwei@pmo.ac.cn

search to the afterglow phase and conducting large-scale searches using X-ray detection satellites such as Chandra¹⁴, Swift X-ray Telescope¹⁵, X-ray Multi-Mirror Mission Newton (XMM-Newton)¹⁶, Advanced Satellite for Cosmology and Astrophysics (ASCA)¹⁷, Satellite per Astronomia X (BeppoSAX)¹⁸, no credible X-ray line feature has been detected in GRBs afterglow^{19–21}.

More recently, a highly significant ($>5\sigma$) narrow emission feature around 10 MeV has been detected in the Fermi data of GRB 221009A^{22,23}. These intriguing features appear during the decay phase of the brightest pulse, with the central energy of the Gaussian distribution gradually shifting towards lower energies over time (about 37 MeV to 6 MeV), while the ratio of the line width to the central energy is nearly constant (about 10%). At the same time, in the Konus-Wind data of GRB 221009A, a similar narrow emission feature has been found with a significance level below 2σ ²⁴. Two independent satellites simultaneously detected the narrow emission feature in GRB 221009A, further bolstering the credibility of the narrow emission feature observed in GRB 221009A.

In this work, we perform a spectral analysis of the prompt emission from GRB 221023A using Fermi Gamma-Ray Burst Monitor (GBM)²⁵ data. We find a marginally significant narrow emission feature around 2.1 MeV. The highest statistical significance of this feature is observed in the time interval 8–30 s, with the chance probability value $<2.56 \times 10^{-5}$ (after accounting for the look-elsewhere effect), corresponding to a Gaussian-equivalent significance $>4.20\sigma$. We find that the relativistic hydrogen-like high-atomic-number ions entrained in the GRB jet can generate such narrow MeV emission lines through the de-excitation of excited electrons.

Results

Light curve and spectral analysis

GRB 221023A triggered the GBM onboard Fermi at 20:41:34.92 UT on 23 October 2022²⁶. Simultaneously, this event was also detected by Konus-Wind²⁷ and AGILE (Astrorivelatore Gamma ad Immagini LEggero)²⁸. The GBM light curve shows one bright peak with a total duration time T_{90} about 39 seconds (s) in the 50–300 keV energy band²⁶, and the fluence reported in the Fermi-GBM catalog is $F = 3.41 \times 10^{-4}$ erg cm⁻² in the energy range 10–1000 keV²⁹. The Fermi Large Area Telescope (LAT)³⁰ instrument was triggered during this event, and the highest-energy photon detected is a 17 GeV event with a 99% probability which is observed 576 seconds after the GBM trigger³¹.

Panels a, b of Fig. 1 presents light curves for GRB 221023A at different energy bands. We analyzed the spectral evolution of the GRB prompt emission by spectra in 5 adjacent time intervals (labelled A (0–5 s), B (5–8 s), C (8–30 s), D (30–36 s) and E (36–60 s)). The spectra of time intervals 0–5 s, 5–8 s, 30–36 s and 36–60 s can be fitted with a Band function (see methods subsection Spectral fitting), detailed analysis results are summarized in Table 1. Interestingly, when fitting the spectra in time interval 8–30 s using the Band function, as shown in the a and b panels of Fig. 2, revealing a distinct narrow and bright emission feature between 1 MeV and 3 MeV. This narrow emission feature can be well modeled by adding a Gaussian component on top of the Band function (see methods subsection Spectral fitting), the best-fit parameter values are $\alpha = -0.93^{+0.01}_{-0.01}$, $E_p = 891.07^{+3.03}_{-33.19}$ keV, $\beta = -2.65^{+0.05}_{-0.02}$, $E_{\text{gauss}} = 2154.60^{+53.37}_{-65.07}$ keV, $\sigma_{\text{gauss}} = 229.36^{+93.57}_{-45.29}$ keV, the c and d panels of Fig. 2 displays the corresponding fitted counts rate and vF_v spectrum. We also present the best-fit vF_v model spectra in 5 adjacent time intervals in Fig. 3. In time interval 8–30 s, comparing models with and without the Gaussian component, we obtained $\Delta\text{AIC} = 51.87$, (BF) = 9.99, and $\Delta\chi^2 = 40.14$, which strongly supports the presence of an additional narrow emission feature (see methods subsection Model comparison). In order to exclude the impact of background subtraction on the extracted spectrum, we calculated the background spectrum by selecting several different time windows. The

result of the narrow emission feature is substantially unaffected (see methods subsection Background).

We performed a time-resolved spectral analysis on time interval 8–30 s to further investigate the presence of the observed feature and to characterize its evolution. We used a fixed window size of 13 s, sliding it in steps of 3 s to divide the time intervals, resulting in four subintervals, referred to as 8–21 s (C.1), 11–24 s (C.2), 14–27 s (C.3), 17–30 s (C.4). In four subintervals, we still extracted the spectra by performing a different selection of the time windows for the background spectrum computation (see methods subsection Background). The narrow emission feature remains clearly visible in these finer time intervals. In the four finer time-resolved spectra (8–21 s, 11–24 s, 14–27 s, 17–30 s), the ΔAIC values vary between 25.76–36.55, the (BF) ranges from 2.06 to 7.34, and the $\Delta\chi^2$ ranges from 18.53 to 34.49. These results further strongly favor adding an additional narrow emission feature (see methods subsection Model comparison). The comprehensive results of the spectral analysis for these four time intervals are presented in Table 1. The temporal evolution of Gaussian component parameters is presented in the (f), (g), and (h) panels of Fig. 1. Notably, the central energy E_{gauss} of the narrow emission feature remains constant at around 2.1 MeV, while the width σ_{gauss} shows a possible decreasing trend over time. The flux of the narrow emission feature is approximately 10^{-6} erg cm⁻² s⁻¹.

Significance analysis

In order to assess the significance of narrow emission features, we created 1.00×10^7 simulated data assuming the Band model and fitted them with both the Band and Band+Gaussian models to obtain the distribution of $\Delta\chi^2$. Table 2 shows the chance probability values ($p\text{-value}_{\text{sim}}$) calculated based on the results of 1.00×10^7 simulations. We also considered the $p\text{-value}_{\text{sim}}$ corrected for the number of independent search trials ($p\text{-value}_{\text{sim-trial}}$). The highest statistical significance of narrow emission features was observed in the time interval C (8–30 s), with the chance probability value $p\text{-value}_{\text{sim}} < 1 \times 10^{-7}$ obtained from results of 1×10^7 simulations, corresponding to a Gaussian-equivalent significance $>5.32\sigma$. Considering the correction for the number of independent search trials, the chance probability value decreases to $p\text{-value}_{\text{sim-trial}} < 2.56 \times 10^{-5}$, corresponding to a Gaussian-equivalent significance $>4.20\sigma$ (see methods subsection Significance calculation of narrow emission feature). The chance probability values for the other time intervals are shown in Table 2.

Comparison with GRB 221009A

The spectral analysis of GRB 221023A reveals a marginally statistically significant narrow emission feature at around 2.1 MeV. This would then represent the second event following GRB 221009A with a narrow emission feature in the MeV energy range. In the case of GRB 221009A, the central energy E_{gauss} of the narrow emission feature decreases over time (about 37 MeV to 6 MeV), while the ratio of the line width to the central energy is nearly constant (about 10%)^{22,23}. For GRB 221023A, we observe the trend: the central energy E_{gauss} remains steady at around 2.1 MeV throughout the observation period, while the width σ_{gauss} exhibits a possible decreasing trend as time progresses, the flux of the narrow emission feature is around 10^{-6} erg cm⁻² s⁻¹. The Fig. 4 displays the lightcurves of GRB 221009A and GRB 221023A within the energy range of 0.2–40 MeV. The shaded regions indicate time intervals in which narrow emission features were detected. The narrow emission feature in GRB 221023A appears during the rising and falling phases of the brightest pulse, with a duration of 22 s (time intervals: 8–30 s) and then disappears. In contrast, the narrow emission feature in GRB 221009A appears during the falling phase of the brightest pulse, with a duration of 100 s (time intervals: 246–256 s and 270–360 s)^{22,23}. Interestingly, the Fe absorption feature previously identified during the prompt emission of GRB 990705 and GRB 011211 appears during the rising phase of the main pulse^{12,13}. This implies a higher likelihood of

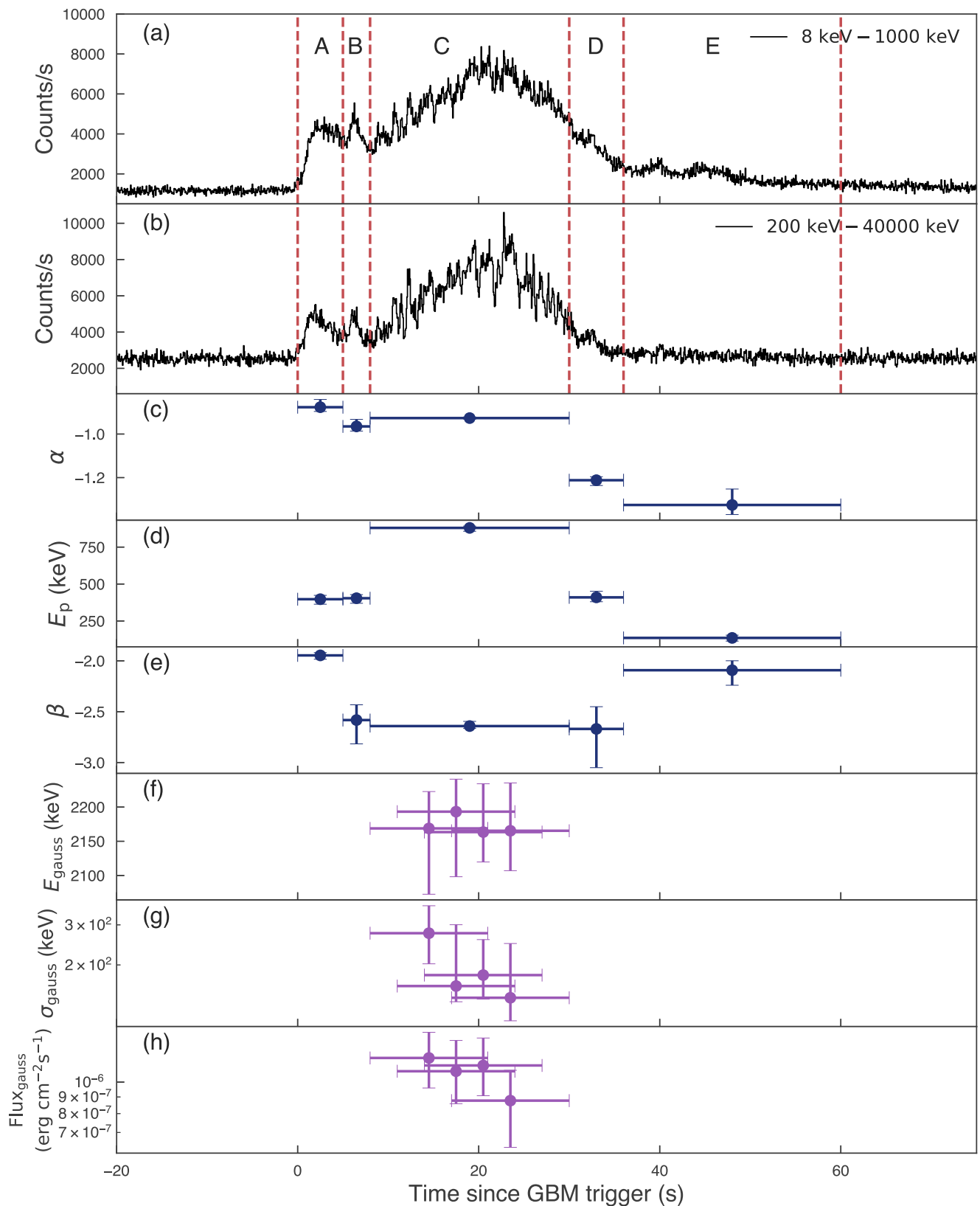


Fig. 1 | Multiwavelength light curves and temporal evolution of spectral parameters. Panels (a) and (b) display the multi-energy band light curves of GRB 221023A observed by Fermi-GBM, with a bin size of 64 ms for each band. The time intervals for spectral analysis are indicated by vertical red dashed lines, labeled as A (0–5 s), B (5–8 s), C (8–30 s), D (30–36 s) and E (36–60 s). Panels (c), (d), and (e) show the temporal evolution of the low-energy spectral index α , peak energy E_p , and high-energy spectral index β of the Band model (deep blue points), respectively. Panels (f), (g) and (h) show the temporal evolution of the central energy E_{gauss} , width σ_{gauss} , and $\text{Flux}_{\text{gauss}}$ of the Gaussian component (purple points), respectively. All error bars represent 1σ uncertainties. Source data are provided as a Source Data file.

and high-energy spectral index β of the Band model (deep blue points), respectively. Panels (f), (g) and (h) show the temporal evolution of the central energy E_{gauss} , width σ_{gauss} , and $\text{Flux}_{\text{gauss}}$ of the Gaussian component (purple points), respectively. All error bars represent 1σ uncertainties. Source data are provided as a Source Data file.

Table 1 | The spectral fitting results for each time interval of GRB 221023A

Time interval (s)	Model	α	E_p (keV)	β	E_{gauss} (keV)	σ_{gauss} (keV)	AIC	$\langle z \rangle$	$\text{Flux}_{\text{total}} \times 10^{-6} (\text{erg cm}^{-2} \text{s}^{-1})$	$\text{Flux}_{\text{gauss}} \times 10^{-6} (\text{erg cm}^{-2} \text{s}^{-1})$
0.00–5.00 [A]	Band	$-0.88^{+0.04}_{-0.02}$	$397.44^{+26.19}_{-33.90}$	$-1.94^{+0.03}_{-0.04}$	3318.89	-716.12	$13.02^{+0.69}_{-0.63}$...
5.00–8.00 [B]	Band	$-0.96^{+0.03}_{-0.02}$	$404.08^{+24.30}_{-34.12}$	$-2.58^{+0.15}_{-0.23}$	2763.77	-594.95	$7.43^{+0.61}_{-0.52}$...
8.00–30.00 [C]	Band	$-0.93^{+0.01}_{-0.01}$	$917.44^{+27.65}_{-16.19}$	$-2.62^{+0.03}_{-0.04}$	5230.40	-1129.88	$23.35^{+0.93}_{-0.92}$...
	Band + Gaussian	$-0.93^{+0.01}_{-0.01}$	$891.07^{+3.03}_{-33.19}$	$-2.65^{+0.05}_{-0.02}$	$2154.60^{+95.37}_{-45.07}$	$229.36^{+95.57}_{-45.29}$	5178.53	-1119.89	$23.50^{+0.33}_{-0.33}$	$1.02^{+0.17}_{-0.16}$
8.00–21.00 [C. 1]	Band	$-0.90^{+0.01}_{-0.01}$	$829.83^{+20.79}_{-23.85}$	$-2.56^{+0.04}_{-0.05}$	4459.59	-970.55	$21.09^{+0.40}_{-0.41}$...
	Band + Gaussian	$-0.90^{+0.01}_{-0.01}$	$789.83^{+18.80}_{-25.03}$	$-2.60^{+0.05}_{-0.05}$	$2168.79^{+53.83}_{-96.16}$	$275.74^{+88.29}_{-73.46}$	4433.83	-966.68	$21.30^{+0.30}_{-0.38}$	$1.21^{+0.23}_{-0.24}$
11.00–24.00 [C. 2]	Band	$-0.90^{+0.01}_{-0.01}$	$982.48^{+26.21}_{-20.41}$	$-2.58^{+0.03}_{-0.05}$	4697.14	-1013.51	$28.43^{+0.45}_{-0.48}$...
	Band + Gaussian	$-0.89^{+0.01}_{-0.01}$	$949.30^{+9.67}_{-37.26}$	$-2.61^{+0.05}_{-0.02}$	$2193.24^{+47.47}_{-56.04}$	$161.00^{+138.96}_{-23.73}$	4660.67	-1006.17	$28.56^{+0.48}_{-0.45}$	$1.08^{+0.25}_{-0.21}$
14.00–27.00 [C. 3]	Band	$-0.91^{+0.01}_{-0.01}$	$1018.00^{+27.50}_{-19.94}$	$-2.58^{+0.02}_{-0.04}$	4541.28	-979.41	$31.04^{+0.47}_{-0.47}$...
	Band + Gaussian	$-0.90^{+0.01}_{-0.01}$	$971.13^{+23.92}_{-21.38}$	$-2.56^{+0.01}_{-0.06}$	$2163.42^{+70.57}_{-43.69}$	$180.45^{+76.01}_{-38.91}$	4504.73	-975.26	$31.14^{+0.49}_{-0.46}$	$1.23^{+0.23}_{-0.21}$
17.00–30.00 [C. 4]	Band	$-0.95^{+0.01}_{-0.01}$	$1026.30^{+29.53}_{-17.21}$	$-2.57^{+0.03}_{-0.04}$	4570.93	-985.95	$29.25^{+0.48}_{-0.48}$...
	Band + Gaussian	$-0.95^{+0.01}_{-0.01}$	$996.46^{+21.54}_{-29.22}$	$-2.54^{+0.07}_{-0.06}$	$2165.34^{+104.96}_{-58.29}$	$143.46^{+104.96}_{-29.83}$	4543.33	-983.89	$29.40^{+0.48}_{-0.48}$	$0.88^{+0.22}_{-0.25}$
30.00–36.00 [D]	Band	$-1.21^{+0.02}_{-0.02}$	$409.88^{+41.10}_{-29.46}$	$-2.67^{+0.22}_{-0.38}$	3398.34	-733.23	$4.66^{+0.44}_{-0.33}$...
36.00–60.00 [E]	Band	$-1.33^{+0.07}_{-0.04}$	$135.48^{+18.45}_{-21.68}$	$-2.09^{+0.09}_{-0.15}$	4644.18	-1007.68	$1.22^{+0.21}_{-0.19}$...

α and β are the low and high energy spectral indices of the Band function respectively. E_p is the peak energy of the Band function νF_ν spectrum. E_{gauss} and σ_{gauss} are the central energy and standard deviation of the Gaussian function. The energy fluxes are calculated between 10 keV and 30 MeV, all errors represent the 1 σ uncertainties.

detecting emission or absorption features during time intervals near the peak of the main pulse in the prompt emission phase of GRBs. It is worth noting that due to the very high photon flux of GRB 221009A, the Fermi-GBM experienced Bad Time Interval (time interval affected by saturation) between 219 and 277 seconds³². It is possible that narrow emission features also exist during the rising phase of the main emission in GRB 221009A.

Discussion

In general, standard models of prompt emission in GRBs do not predict the appearance of a transient MeV narrow emission component^{23,34}. To explain our potential finding, we have explored several possible scenarios. One possible explanation for the narrow emission feature is the blue-shifted annihilation line of relatively cold ($k_B T \ll m_e c^2$, where k_B is Boltzmann constant, T is the temperature of the medium, m_e is the mass of the electron, and c is the speed of light) electron-positron pairs. Within the emission region (resulting from internal shocks and/or magnetic reconnection) of GRB, electron-positron pairs are readily formed within the GRB jet (such as two-photon pair production $\gamma\gamma \rightarrow e^+e^-$ ^{2,33}). Numerical simulations of GRB spectra indicate that the generated spectra depend on the compactness of the fireball. In scenarios with high compactness, electron-positron pairs play an essential role in shaping the GRB prompt emission spectrum. In a pair-dominated fireball, a pair annihilation line is predicted^{35,36}. In the observer frame, a line is expected to appear at an energy of $E_{\text{line}} = \Gamma m_e c^2 / (1+z)$, where Γ is the bulk Lorentz factor of the emitting region and z represents the redshift. For the typical energy E_{line} is about 2.1 MeV of the observed lines in GRB 221023A, the bulk Lorentz factor of the emitting region is required to be Γ is about $4(1+z)$. Considering a redshift of $z = 2$, the bulk Lorentz factor Γ is about 12. In this scenario, how such a low bulk Lorentz factor is generated and maintained for an extended period in the prompt emission of the GRB is an issue.

The second scenario involves the possibility that the narrow emission feature is an intrinsic low-energy spectral line (such as the 6.4 keV fluorescent K- α iron line). This spectral line may be emitted within the region associated with the supernova ejecta. Subsequently, the energy of the spectral line could be boosted through up-scattering by the relativistic jet. The spectral line feature identified in GRB 221023A is narrow, which implies that electrons scattering photons are cold. This form of bulk Comptonization has already been proposed to occur within blazar jets³⁷. The boosted photon energy of the low-energy spectral line is $E_{\text{line}} = \Gamma^2 E_{\text{low}} / (1+z)$, where Γ is the jet bulk Lorentz factor and E_{low} represents the low-energy spectral line of the particular element. If the observed spectral feature in GRB 221023A arises from the 6.4 keV iron K- α line, and the typical photon energy of the observed line is around 2.1 MeV, this would require a jet bulk Lorentz factor Γ to be about $18(1+z)^{1/2}$. Considering a redshift of $z = 2$, the bulk Lorentz factor Γ is about 31. This scenario faces the same issue as the first one, namely, the low bulk Lorentz factor problem.

The third possible scenario is that the narrow emission feature may originate from MeV nuclear de-excitation lines. The energetic particles interacting with ambient matter could excite heavy nuclei which can emit MeV γ -ray line emissions via de-excitation, such as the 4.44 MeV line from ^{12}C and the 6.13 MeV line from ^{16}O ^{38–40}. In fact, nuclear de-excitation line emissions from ^{12}C and ^{16}O have been observed in solar flares^{41–43}. Moreover, the existence of such nuclear de-excitation line has long been anticipated to be found within supernova remnants^{44–47}. The observed photon energy of the nuclear de-excitation line is $E_{\text{line}} = E_{\text{element}} / (1+z)$, where z is the redshift, and E_{element} corresponds to the energy of the particular element's nuclear de-excitation line. If we assume that the narrow emission feature in GRB 221023A arises from nuclear de-excitation lines of ^{12}C or ^{16}O , it corresponds to redshifts of $z = 1.1$ or $z = 1.9$, respectively. However, the radiation from the nuclear de-excitation

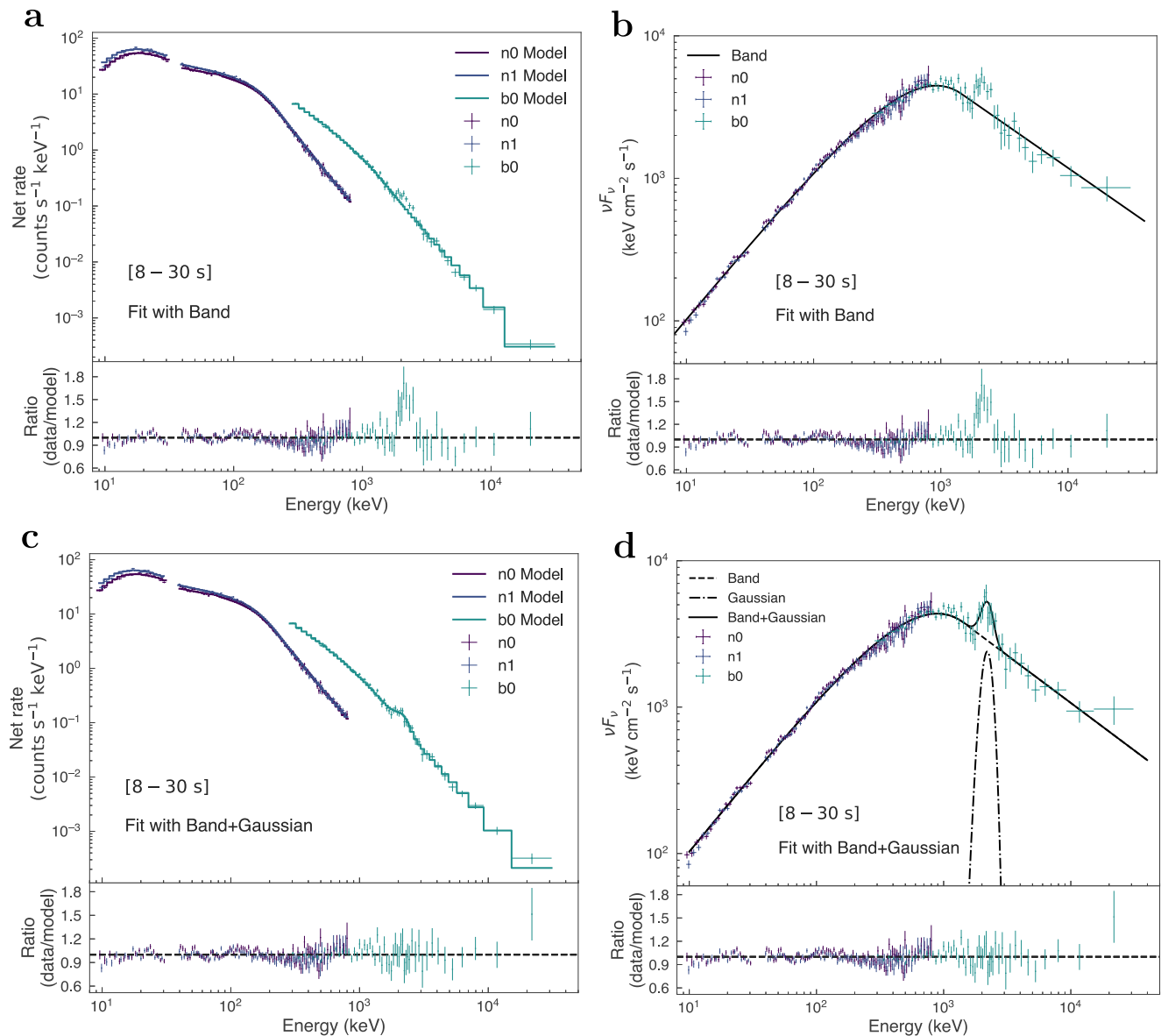


Fig. 2 | Spectral fitting within the 8–30 s time interval. The counts rate spectrum in the panel **a** and the νF_ν spectrum in the panel **b** are obtained from fitting the Band function. Data are from GBM's two sodium iodide (NaI) detectors (n0: dark purple, n1: blue) and one BGO detector (b0: light cyan-green). The narrow feature appears

as an excess around 1 MeV–3 MeV in the b0 detector data. Panels **c** and **d** show the same spectra fitted with the Band function plus a Gaussian component to model the observed excess. Error bars indicate the 1σ uncertainty on data points. Source data are provided as a Source Data file.

of the ambient matter is almost isotropic, while the gamma-ray burst is collimated. Therefore, the energy budget needed to generate such a MeV emission line would be larger than the energy of the prompt emission for a typical half-opening angle $\theta_j = 0.1$ rad. Note that for a large θ_j , such as $\theta_j > 0.3$ rad, this energy problem can be alleviated.

The fourth possible scenario is that the heavy nuclei, especially relativistic hydrogen-like high-atomic-number ions originating from the β decay of unstable nuclei and/or the recombination, entrained in GRB jets can produce such a narrow MeV emission line via electron de-excitation⁴⁸. In this model, the reflection of the radiation from the WR star can generate enough seed photons to excite electrons. After the jet with heavy nuclei breaks through the photosphere and hydrogen-like heavy ions are generated by β decay and/or recombination, the emission line can be generated. The emission lines occur at an energy of $E_{\text{line}} = \Gamma \epsilon_z / (1+z)$, where $\epsilon_z = m_e \alpha^2 c^2 Z^2 / 2$ is the Rydberg energy, α is the fine-structure constant, and $Z = 29$ is the atomic number of the copper. Note that we take copper as an example here since it can satisfy the

half-life requirement of the model. This model can explain the MeV emission line of GRB 221023A well with reasonable parameters. We assume the half-opening angle θ_j of the GRB jet is about 0.1 rad and the redshift $z = 0.1$, we estimate that the jet beaming-corrected gamma-ray emission energy of GRB 221023A is about 7×10^{49} erg. Considering the propagation distance $d = 4.8 \times 10^{11}$ cm, which corresponds to the timescale without an observable MeV emission line at the beginning, the Lorentz factor of the jet, $\Gamma = (1+z)E_{\text{line}}/\epsilon_z$, is about 300. The total mass of heavy nuclei entrained in the GRB jet is $M_{\text{tot, nuclei}} = \theta_j^2 c m_i \epsilon_{\text{line}} / (4E_{\text{line}} \Gamma_e d \zeta_i)$ approximately 10^{26} g. Here, ϵ_{line} is the observed isotropic total energy of the emission line, Γ_e is the total excitation rate for an electron of the high-Z ion transitioned from the ground in the lab frame, m_i is the mass of the high-Z ion (i.e., the copper), and $\zeta_i = 0.1$ means the mass fraction capable of producing emission lines relative to the mass of all nuclei entrained in the GRB jet⁴⁸. We find the kinetic energy of heavy nuclei in the jet is about 3×10^{49} erg, which is much larger than the energy budget of the observed emission line, approximately 3×10^{48} erg.

Methods

Fermi data analysis

The GBM consists of 12 sodium iodides (NaI) detectors (8 keV–1 MeV) and two bismuth germanate (BGO) detectors (20 keV–40 MeV)²⁵, which has three different data types: continuous time (CTIME), continuous spectroscopy (CSPEC) and time-tagged event (TTE). The CTIME data include eight energy channels and have a finer time resolution of 64 ms. The CSPEC data include 128 energy channels, with a time resolution of 1.024 s. The TTE data consists of individual detector events, each tagged with arrival time, energy (128 channels), and detector number²⁵. We download the GBM data of GRB 221023A from the public science support center at the official Fermi Website <https://heasarc.gsfc.nasa.gov/FTP/fermi/data/gbm/triggers/2022/bn221023862/>.

We extracted spectrum by using the TTE data from the brightest (with the smallest angle between this detector and the source object) two NaI detectors (n0, n1) and one BGO detectors (b0). The light curves were extracted using the GBM Data Tools⁴⁹. The spectral analysis of the Fermi-GBM data was performed using the Bayesian approach package, namely the Multi-Mission Maximum Likelihood Framework (3ML)⁵⁰. We selected the GBM spectrum over 8–900 keV and 0.3–30 MeV for NaI detectors and BGO detector, respectively. In order to avoid the iodine K-edge at 33.17 keV²⁵, we ignore the data for the 30–40 keV energy ranges. The background spectrum from the GBM data was extracted from the CSPEC data with two time intervals before and after the prompt emission phase and modeled with a polynomial function of order 0–4 (Selected background time

intervals: –130–10 s, 100–200 s). We have used the Bayesian fitting method for the spectral fitting, and the sampler is set to the dynesty-nested. And we accounted for intercalibration constant factors among NaI and BGO detectors.

Spectral fitting

Figure 1 presents the light curves for GRB 221023A at different energy band. We subdivided the light curve into five intervals labeled A (0–5 s), B (5–8 s), C (8–30 s), D (30–36 s) and E (36–60 s), respectively, which were separated by red dashed vertical lines. We fit the corresponding spectra using the empirical Band function⁴, formulated as follows:

$$N_{\text{Band}}(E) = K \begin{cases} \left(\frac{E}{100 \text{ keV}}\right)^{\alpha} \exp\left(-\frac{E(2+\alpha)}{E_p}\right), & \left(\text{if } E < (\alpha - \beta) \frac{E_p}{2+\alpha}\right) \\ \left[\frac{(\alpha - \beta)E_p}{(2+\alpha)100 \text{ keV}}\right]^{\alpha - \beta} \exp(\beta - \alpha) \left(\frac{E}{100 \text{ keV}}\right)^{\beta}, & \left(\text{if } E \geq (\alpha - \beta) \frac{E_p}{2+\alpha}\right) \end{cases} \quad (1)$$

where K is the normalization of Band spectrum, α and β are the low and high-energy photon spectral indices, respectively. E is the observational photon energy, and E_p is the peak energy of the νF_{ν} spectrum. The maximum values of the marginalized posterior probability densities and the corresponding 1σ uncertainties for each parameter of the Band model in each time interval are presented in Table 1.

The intriguing aspect was the shape of the spectrum in the time interval 8–30 s, as shown in the a and b panels of Fig. 2, revealing a distinct narrow and bright emission feature between 1 MeV and 3 MeV, this feature did not appear in the other four spectra. We further analyzed the GRBs data detected by the Fermi satellite within ten days before and after the explosion of GRB 221023A. For each of these events, we performed time-resolved spectral analysis using different signal-to-noise ratios and Bayesian blocks, no similar narrow feature were found in these GRBs. In order to model the narrow emission feature observed at MeV energies, we incorporated a blackbody component into the Band function. However, Blackbody component is not enough narrow to properly fit the narrow emission feature. Therefore, we introduced an additional Gaussian component to fit the spectrum of the time interval 8–30 s. The Gaussian function is defined as follows:

$$N_{\text{gauss}}(E) = A \frac{1}{\sigma_{\text{gauss}} \sqrt{2\pi}} \exp\left(\frac{-(E - E_{\text{gauss}})^2}{2(\sigma_{\text{gauss}})^2}\right). \quad (2)$$

where A is the normalization of spectrum, E_{gauss} and σ_{gauss} are the central energy and standard deviation of the Gaussian function. We have found that the Gaussian component is well constrained at $E_{\text{gauss}} = 2154.60^{+53.37}_{-65.07}$ keV, with a width $\sigma_{\text{gauss}} = 229.36^{+93.57}_{-45.29}$ keV. The fitting results of the spectrum are presented in Table 1. The c and d panels of Fig. 2 displays the counts rate and νF_{ν} spectrum, with fitting using the Band function plus a Gaussian component. From the light

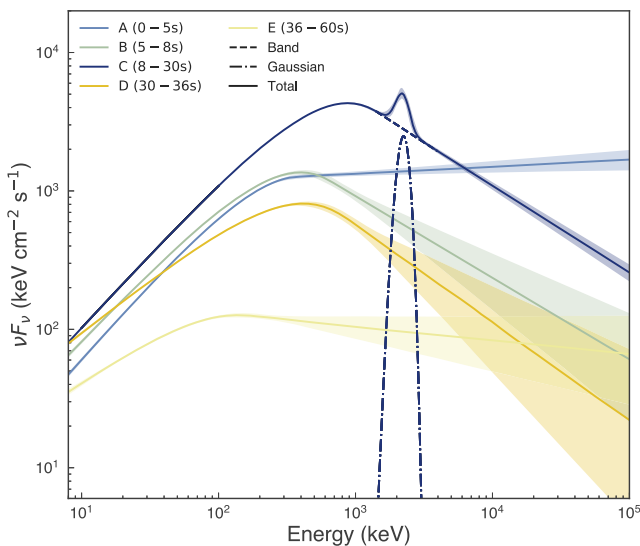


Fig. 3 | Energy spectrum evolution. Best-fit νF_{ν} model spectra for the time-resolved data in different time intervals, five time intervals are color-coded, with the corresponding shaded colors show the 68% confidence levels.

Table 2 | The results of evaluating the significance

Time interval (s)	8.00–30.00 [C]	8.00–21.00 [C. 1]	11.00–24.00 [C. 2]	14.00–27.00 [C. 3]	17.00–30.00 [C. 4]
ΔAIC	51.87	25.76	36.47	36.55	27.60
$\ln(\text{BF})$	9.99	3.87	7.34	4.15	2.06
$\Delta\chi^2$	40.14	34.49	27.09	30.46	18.53
$p\text{-value}_{\text{sim}}$	$<1.00 \times 10^{-7}$	1.00×10^{-7}	6.30×10^{-6}	1.00×10^{-6}	7.69×10^{-4}
	($>5.32\sigma$)	(5.32σ)	(4.51σ)	(4.89σ)	(3.36σ)
$p\text{-value}_{\text{sim-trial}}$	$<2.56 \times 10^{-5}$	2.56×10^{-5}	1.61×10^{-3}	2.56×10^{-4}	1.79×10^{-1}
	($>4.20\sigma$)	(4.20σ)	(3.15σ)	(3.65σ)	(1.34σ)

ΔAIC is the AIC value of the Band model minus the AIC value of the Band+Gaussian model. BF is the Bayes factor. $\Delta\chi^2$ is the statistical difference in the goodness-of-fit between the models Band and Band+Gaussian. The $p\text{-value}_{\text{sim}}$ is the chance probability value obtained from 1.00×10^7 simulations. The $p\text{-value}_{\text{sim-trial}}$ is the corrected values obtained by accounting for the number of independent search trials based on $p\text{-value}_{\text{sim}}$. The values in parentheses correspond to the Gaussian-equivalent significance.

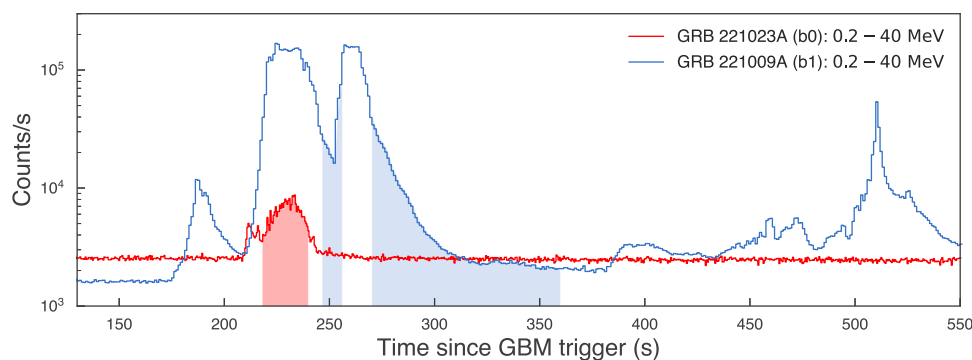


Fig. 4 | Comparison of light curve. Comparison of the light curves of GRB 221023A (red) and GRB 221009A (blue) in the energy range of 0.2–40 MeV, with the corresponding shaded colors regions showing the time intervals where narrow emission

features were detected. The trigger time of GRB 221023A was shifted backward by 210 s. Source data are provided as a Source Data file.

Table 3 | Energy spectrum resulted from different time windows selected for the background region in time interval C (8–30 s)

Background selection regions (s)	E_{gauss} (keV)	σ_{gauss} (keV)	ΔAIC
–98 to –20, 90–180	$2146.06^{+67.56}_{-53.45}$	$189.89^{+128.11}_{-9.18}$	48.48
–150 to –60, 150–200	$2175.97^{+18.86}_{-79.49}$	$210.85^{+80.14}_{-47.54}$	57.71
–290 to –10, 85–300	$2158.45^{+49.76}_{-61.89}$	$202.85^{+99.60}_{-36.32}$	51.58

E_{gauss} and σ_{gauss} are the central energy and standard deviation of the Gaussian function. ΔAIC is the AIC value of the Band model minus the AIC value of the Band+Gaussian model. All errors represent the 1σ uncertainties.

curve presented in the (a) and (b) panel of Fig. 1, the MeV narrow emission feature appears during the rising and falling phases of the main pulse. When compared to other time intervals (0–5 s, 5–8 s, 30–36 s and 36–60 s), the time interval 8–30 s exhibits the highest flux and the best signal-to-noise ratio. The evolution of the spectral parameters of the Band function in the best-fit model is shown in the (c), (d), and (e) panels of Fig. 1. The low-energy spectral index α evolved from –0.88 to –1.33, indicating an evolution from hard to soft. Additionally, the peak energy E_p varies between 397 keV and 920 keV, showing the pattern of intensity tracking⁵¹.

For the A (0–5 s), B (5–8 s), D (30–36 s) and E (36–60 s) time intervals, we fixed the line width at $\sigma_{\text{gauss}} = 200$ keV and the line central energy at $E_{\text{gauss}} = 2.1$ MeV in the likelihood fit, thereby deriving the upper limits on the flux of the narrow emission feature, which are $\text{Flux}_{\text{gauss}} < 5.1 \times 10^{-7} \text{ erg cm}^{-2} \text{ s}^{-1}$, $\text{Flux}_{\text{gauss}} < 3.2 \times 10^{-7} \text{ erg cm}^{-2} \text{ s}^{-1}$, $\text{Flux}_{\text{gauss}} < 2.4 \times 10^{-7} \text{ erg cm}^{-2} \text{ s}^{-1}$, and $\text{Flux}_{\text{gauss}} < 9.9 \times 10^{-8} \text{ erg cm}^{-2} \text{ s}^{-1}$, respectively.

Model comparison

We employed three different methods to assess the necessity of adding a Gaussian component to the prompt gamma-ray spectrum of GRB 221023A.

The Akaike Information Criterion (AIC) is employed for model comparison when penalizing additional free parameters is necessary to prevent overfitting. The AIC is formulated as the logarithm of the likelihood with a penalty term^{52,53}:

$$\text{AIC} = -2\ln(\mathcal{L}(d|\theta)) + 2\theta. \quad (3)$$

where $\mathcal{L}(d|\theta)$ is the likelihood of the model, θ is the number of free parameters of a particular model. The model with the smallest AIC is favored. $\Delta\text{AIC} = \text{AIC}_{\text{Band}} - \text{AIC}_{\text{Band+Gaussian}}$ provides a numerical assessment of the evidence that model Band+Gaussian is to be preferred over model Band. When $\Delta\text{AIC} > 10$, it strongly favors the model

Band+Gaussian. As shown in Table 2, our results reveal that during the time interval 8–30 s, the ΔAIC value reaches its maximum at 51.87, strongly favoring the Gaussian+Band model over the simpler Band model. In the four finer time-resolved spectra (8–21 s (C.1), 11–24 s (C.2), 14–27 s (C.3), 17–30 s (C.4)), the ΔAIC values vary between 25.76 and 36.55, further strongly favoring the addition of the Gaussian component.

When evaluating the significance of emission or absorption features in spectrum analysis, the Bayesian factor is also a commonly used tool^{20,54,55}. The Bayesian factor is utilized to compare the relative support for different models, serving as a measure to evaluate the strength of evidence in favor of one model over another. Bayesian evidence (\mathcal{Z}) is calculated for model selection and can be formulated as follows:

$$\mathcal{Z} = \int \mathcal{L}(d|\theta)\pi(\theta)d\theta, \quad (4)$$

where $\pi(\theta)$ represents the prior distribution for θ . The ratio of the Bayesian evidence for two different models is called the Bayes factor (BF). In this paper, the BF is formulated as follows:

$$\text{BF} = \frac{\mathcal{Z}_{\text{Band+Gaussian}}}{\mathcal{Z}_{\text{Band}}}, \quad (5)$$

The corresponding logarithmic expression is as follows:

$$\ln(\text{BF}) = \ln(\mathcal{Z}_{\text{Band+Gaussian}}) - \ln(\mathcal{Z}_{\text{Band}}). \quad (6)$$

If $\ln(\text{BF}) > 8$, it indicates strong evidence in favor of the Band+Gaussian model^{56,57}. We calculated the Bayes factors for time intervals with narrow emission features (as shown in Table 2), and the results shown that the Band+Gaussian model was preferred in finer time intervals (8–21 s, 11–24 s, 14–27 s, 17–30 s) with (BF) between 2.06–7.34. Remarkably, during the entire time interval of 8–30 s, the (BF) = 9.99 providing strong statistical support for the addition of the Gaussian component, suggesting the presence of the narrow emission feature.

We also employed the alternative analysis software GTBURST to extract the corresponding spectra from the time intervals exhibiting a narrow emission feature. The extracted spectra were fitted using the XSPEC 12.11.1⁵⁸, and the fitting results similarly indicate the presence of distinct narrow and bright emission feature between 1 MeV and 3 MeV. $\Delta\chi^2$ represents the statistical difference in the goodness-of-fit between the models Band and Band+Gaussian, the $\Delta\chi^2$ values are displayed in Table 2. The highest $\Delta\chi^2$ value of 40.14 was observed in the time interval 8–30 s, while the $\Delta\chi^2$ values for the other time intervals ranged from 18.53 to 34.49.

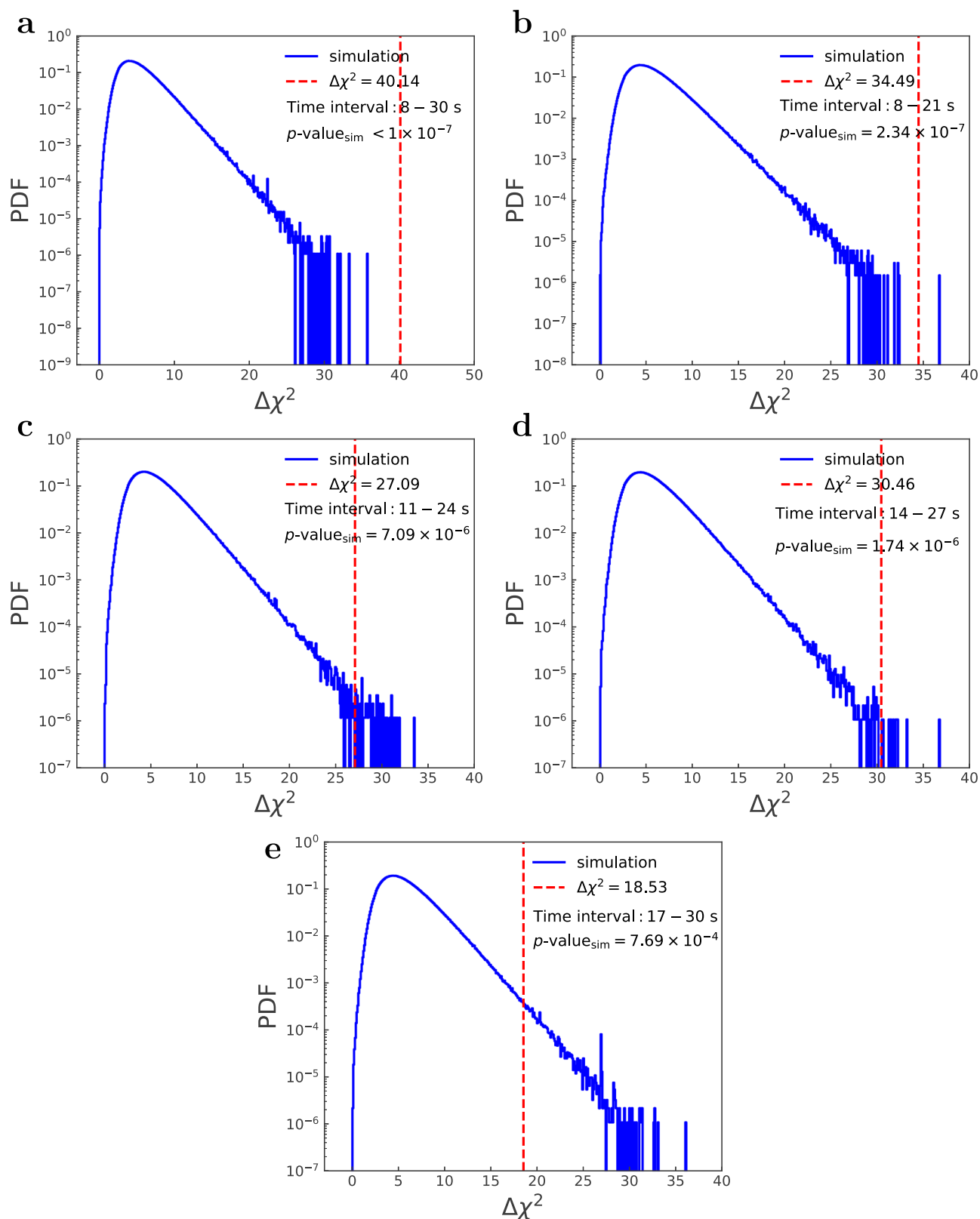


Fig. 5 | Simulated $\Delta\chi^2$ distribution. $\Delta\chi^2$ is the statistical difference in the goodness-of-fit between the models Band and Band+Gaussian. The Panels **a**, **b**, **c**, **d**, and **e** show the probability distribution function (PDF) of $\Delta\chi^2$ values obtained from 1×10^7 simulations for time intervals 8 – 30 s, 8 – 21 s, 11 – 24 s, 14 – 27 s, 17 – 30 s,

respectively. The red dashed line represents the observed $\Delta\chi^2$ value. The $p\text{-value}_{\text{sim}}$ is the chance probability value obtained from 1.00×10^7 simulations. If after N simulations no $\Delta\chi^2$ value exceeds the actual fitting result, we report $p\text{-value}_{\text{sim}} < 1/N$. Source data are provided as a Source Data file.

Background

The selection of time intervals for background subtraction can also impact the analysis of the source spectrum. In order to assess the impact of background subtraction on extracted spectrum.

In time interval 8 – 30 s, we calculated the background spectrum by selecting several different time windows. Even with this approach, the narrow emission features are still clearly visible. We performed both Band and Band + Gaussian fittings in the spectra extracted by subtracting different backgrounds in time interval 8 – 30 s. As shown in Table 3, The central energy E_{gauss} of the narrow emission feature are all around 2.1 MeV and the widths σ_{gauss} are all around 200 keV, and the values of the ΔAIC are around 50. The result of the narrow Gaussian feature is substantially unaffected.

In four subintervals (8 – 21 s (C.1), (11 – 24 s (C.2), 14 – 27 s (C.3), 17 – 30 s (C.4)), we extracted the spectra by performing a different selection of the time windows for the background spectrum computation, the background time intervals selected for each time intervals, for 8 – 21 s: –200 – –40 s, 120 – 250 s; for 11 – 24 s: –90 – –10 s, 100 – 150 s; for 14 – 27 s: –90 – –20 s, 180 – 250 s; for 17 – 30 s: –200 – –50 s, 120 – 250 s.

Significance calculation of narrow emission feature

We calculated the chance probability value (p -value) of the narrow emission feature through spectral simulation. The spectral simulation across the entire energy range (10 keV – 30 MeV) is performed using the fakeit command in XSPEC. These simulations are based on the parameters obtained from fitting the actual data using the Band model. The tclout simpars (based on the covariance matrix at the best fit) command in XSPEC is used to generate randomized model parameters before each simulation. The total number of spectral simulations N is 1.00×10^7 . For each simulated spectra, we perform both Band and Band+Gaussian fittings (search for Gaussian components across the entire energy range of 10 keV to 30 MeV) and record the maximum $\Delta\chi^2$ value^{20,55}. Finally, we assess the significance of the narrow emission feature by analyzing the $\Delta\chi^2$ values recorded in Tables 2. The p -value represents the fraction of simulated $\Delta\chi^2_i$ values that exceeds the observed $\Delta\chi^2$ value:

$$p\text{-value}_{\text{sim}} = n[\Delta\chi^2_i \geq \Delta\chi^2] / N. \quad (7)$$

If after N simulations we still do not obtain a $\Delta\chi^2$ value exceeding the observed value, we report $p\text{-value}_{\text{sim}} < 1/N$. The probability distribution function (PDF) of $\Delta\chi^2$ values obtained from 1×10^7 simulations for different time intervals are shown in Fig. 5.

In the process of calibrating the $\Delta\chi^2$ test distribution through simulation, the intensity, location and width of the line, are not fixed to predetermined values but are allowed to vary freely during the fit. This is a standard setup when performing the simulation. The number of independent search trials conducted by dividing multiple time intervals in the time series of different GRBs must be considered (the look-elsewhere effect⁵⁹). The chance probability value $p\text{-value}_{\text{sim-trial}}$ after considering the correction for the number of independent search trials on the basis of the $p\text{-value}_{\text{sim}}$ is^{59–61}:

$$p\text{-value}_{\text{sim-trial}} = 1 - (1 - p\text{-value}_{\text{sim}})^t. \quad (8)$$

where t is the number of independent search trials. We searched for GRBs spectral lines from the Fermi-GBM catalog (<https://heasarc.gsfc.nasa.gov/W3Browse/fermi/fermigbrst.html>) in descending order of fluence²⁹. We excluded GRB 221009A, which already has identified narrow emission features^{22,23}. The extreme brightness of GRB 130427A and GRB 230307A caused detector pile-up effects, so we excluded the saturated time intervals of 4.5 – 11.5 s for GRB 130427A and 3 – 7 s for GRB 230307A^{62,63}. We searched a total of 9 GRBs, for each burst, time

intervals were divided based on BGO light curve signal-to-noise ratio greater than 40. This resulted in a total of 256 searches. Therefore, the number of independent search trials $t = 256$.

We found the highest statistical significance of narrow emission feature in the time interval 8 – 30 s, with the chance probability value $p\text{-value}_{\text{sim}} < 1 \times 10^{-7}$ obtained from results of 1.00×10^7 simulations, corresponding to the Gaussian-equivalent significance $> 5.32\sigma$. Considering the correction for the number of independent search trials, the chance probability value decreases to $p\text{-value}_{\text{sim-trial}} < 2.56 \times 10^{-5}$, corresponding to the Gaussian-equivalent significance $> 4.20\sigma$. The chance probability values for the other time intervals are shown in Table 2.

Data availability

The Fermi-GBM data for GRB 221023A and GRB 221009A used in this paper are publicly available at <https://heasarc.gsfc.nasa.gov/FTP/fermi/data/gbm/triggers/2022/bn221023862/> and <https://heasarc.gsfc.nasa.gov/FTP/fermi/data/gbm/triggers/2022/bn221009553/>. These data were obtained from the High Energy Astrophysics Science Archive Research Center (HEASARC) at NASA's Goddard Space Flight Center. The Fermi-GBM Gamma-Ray Burst catalog is available at <https://heasarc.gsfc.nasa.gov/W3Browse/fermi/fermigbrst.html>. The datasets generated during and/or analyzed during the current study are available from the corresponding author upon request. Source data are provided with this paper.

Code availability

The GTBURST package for analyzing the Fermi-GBM Gamma-Ray Burst data are publicly available at <https://fermi.gsfc.nasa.gov/ssc/data/analysis/scitools/gtburst.html>. XSPEC is available at <https://heasarc.gsfc.nasa.gov/xanadu/xspec/>. 3ML is available at <https://threeml.readthedocs.io/en/stable/>. Fermi-GBM Data Tools is available at https://fermi.gsfc.nasa.gov/ssc/data/analysis/gbm/gbm_data_tools/gdt-docs/notebooks/Trigdat.html.

References

- Rees, M. J. & Meszaros, P. Unsteady Outflow Models for Cosmological Gamma-Ray Bursts. *Astrophys. J. Lett.* **430**, L93 (1994).
- Zhang, B. & Yan, H. The Internal-collision-induced Magnetic Reconnection and Turbulence (ICMART) Model of Gamma-ray Bursts. *Astrophys. J.* **726**, 90 (2011).
- Pe'er, A. Physics of Gamma-Ray Bursts Prompt Emission. *Adv. Astron.* **2015**, 907321 (2015).
- Band, D. et al. BATSE Observations of Gamma-Ray Burst Spectra. I. Spectral Diversity. *Astrophys. J.* **413**, 281 (1993).
- Mazets, E. P., Golenetskij, S. V., Aptekar, R. L., Guryan, Y. A. & Ilinskij, V. N. Lines in the energy spectra of gamma-ray bursts. *Pisma v. Astronomicheskii Zh.* **6**, 706–711 (1980).
- Mazets, E. P., Golenetskij, S. V., Aptekar, R. L., Gurian, I. A. & Ilinskij, V. N. Cyclotron and annihilation lines in γ -ray bursts. *Nature* **290**, 378–382 (1981).
- Hueter, G. J. & Gruber, D. E. An absorption feature in the spectrum of a gamma ray burst on 25 March 1978. In Brinkmann, W. & Truemper, J. (eds.) *Accreting Neutron Stars*, 213–215 (1982).
- Hueter, G. J. Observation of an absorption feature in a gamma ray burst spectrum. In Woosley, S. E. (ed.) *High Energy Transients in Astrophysics*, vol. 115 of *American Institute of Physics Conference Series*, 373–377 (1984).
- Murakami, T., Fujii, M., Hayashida, K., Itoh, M. & Nishimura, J. Evidence for cyclotron absorption from spectral features in gamma-ray bursts seen with Ginga. *Nature* **335**, 234–235 (1988).
- Yoshida, A., Murakami, T., Nishimura, J., Kondo, I. & Fenimore, E. E. A New Detection of Cyclotron Lines Seen in a Gamma-Ray Burst GB890929. *PASJ* **43**, L69–L75 (1991).

11. Yoshida, A., Murakami, T., Nishimura, J., Kondo, I. & Fenimore, E. E. Cyclotron lines observed with GINGA. In Ho, C., Epstein, R. I. & Fenimore, E. E. (eds.) *Gamma-Ray Bursts - Observations, Analyses and Theories*, 399–406 (1992).
12. Amati, L. et al. Discovery of a Transient Absorption Edge in the X-ray Spectrum of GRB 990705. *Science* **290**, 953–955 (2000).
13. Frontera, F. et al. The Prompt X-Ray Emission of GRB 011211: Possible Evidence of a Transient Absorption Feature. *Astrophys. J.* **616**, 1078–1085 (2004).
14. Weisskopf, M. C., Tananbaum, H. D., Van Speybroeck, L. P. & O'Dell, S. L. Chandra X-ray Observatory (CXO): overview. In Truemper, J. E. & Aschenbach, B. (eds.) *X-Ray Optics, Instruments, and Missions III*, vol. 4012 of *Society of Photo-Optical Instrumentation Engineers (SPIE) Conference Series*, 2–16 (2000).
15. Burrows, D. N. et al. The Swift X-Ray Telescope. *Space Sci. Rev.* **120**, 165–195 (2005).
16. Jansen, F. et al. XMM-Newton observatory. I. The spacecraft and operations. *Astron. Astrophys.* **365**, L1–L6 (2001).
17. Tanaka, Y., Inoue, H. & Holt, S. S. The X-Ray Astronomy Satellite ASCA. *PASJ* **46**, L37–L41 (1994).
18. Boella, G. et al. BeppoSAX, the wide band mission for X-ray astronomy. *AAS* **122**, 299–307 (1997).
19. Sako, M., Harrison, F. A. & Rutledge, R. E. A Search for Discrete X-Ray Spectral Features in a Sample of Bright γ -Ray Burst Afterglows. *Astrophys. J.* **623**, 973–999 (2005).
20. Hurkett, C. P. et al. Line Searches in Swift X-Ray Spectra. *Astrophys. J.* **679**, 587–606 (2008).
21. Campana, S. et al. Searching for narrow absorption and emission lines in XMM-Newton spectra of gamma-ray bursts. *Astron. Astrophys.* **592**, A85 (2016).
22. Ravasio, M. E. et al. A mega-electron volt emission line in the spectrum of a gamma-ray burst. *Science* **385**, 452–455 (2024).
23. Zhang, Y.-Q. et al. Observation of spectral lines in the exceptional GRB 221009A. *Sci. China Phys., Mech., Astron.* **67**, 289511 (2024).
24. Frederiks, D. et al. Properties of the Extremely Energetic GRB 221009A from Konus-WIND and SRG/ART-XC Observations. *Astrophys. J. Lett.* **949**, L7 (2023).
25. Meegan, C. et al. The Fermi Gamma-ray Burst Monitor. *Astrophys. J.* **702**, 791–804 (2009).
26. Dunwoody, R., Mangan, J., Meegan, C. & Fermi GBM Team. GRB 221023A: Fermi GBM Observation. *GRB Coord. Netw.* **32845**, 1 (2022).
27. Ridhaia, A. et al. Konus-Wind detection of GRB 221023A. *GRB Coord. Netw.* **32849**, 1 (2022).
28. Ursi, A. et al. GRB 221023A: AGILE detection of a burst. *GRB Coord. Netw.* **32825**, 1 (2022).
29. von Kienlin, A. et al. The Fourth Fermi-GBM Gamma-Ray Burst Catalog: A Decade of Data. *Astrophys. J.* **893**, 46 (2020).
30. Atwood, W. B. et al. The Large Area Telescope on the Fermi Gamma-Ray Space Telescope Mission. *Astrophys. J.* **697**, 1071–1102 (2009).
31. Pilleri, R. et al. GRB 221023A: Fermi-LAT detection. *GRB Coord. Netw.* **32831**, 1 (2022).
32. Lesage, S. et al. Fermi-GBM Discovery of GRB 221009A: An Extraordinarily Bright GRB from Onset to Afterglow. *arXiv e-prints arXiv:2303.14172* (2023).
33. Rees, M. J. & Meszaros, P. Unsteady outflow models for cosmological gamma-ray bursts. *Astrophys. J. Lett.* **430**, L93–L96 (1994).
34. Drenkhahn, G. & Spruit, H. C. Efficient acceleration and radiation in Poynting flux powered GRB outflows. *Astron. Astrophys.* **391**, 1141–1153 (2002).
35. Pe'er, A. & Waxman, E. Prompt Gamma-Ray Burst Spectra: Detailed Calculations and the Effect of Pair Production. *Astrophys. J.* **613**, 448–459 (2004).
36. Pe'er, A., Mészáros, P. & Rees, M. J. The Observable Effects of a Photospheric Component on GRB and XRF Prompt Emission Spectrum. *Astrophys. J.* **642**, 995–1003 (2006).
37. Sikora, M., Begelman, M. C. & Rees, M. J. Comptonization of Diffuse Ambient Radiation by a Relativistic Jet: The Source of Gamma Rays from Blazars? *Astrophys. J.* **421**, 153 (1994).
38. Ramaty, R., Kozlovsky, B. & Lingenfelter, R. E. Nuclear gamma-rays from energetic particle interactions. *Astrophys. J. Suppl. Ser.* **40**, 487–526 (1979).
39. Murphy, R. J., Dermer, C. D. & Ramaty, R. High-Energy Processes in Solar Flares. *Astrophys. J. Suppl. Ser.* **63**, 721 (1987).
40. Murphy, R. J., Kozlovsky, B., Kiener, J. & Share, G. H. Nuclear Gamma-Ray De-Excitation Lines and Continuum from Accelerated-Particle Interactions in Solar Flares. *Astrophys. J. Suppl. Ser.* **183**, 142–155 (2009).
41. Chupp, E. L. et al. Solar Gamma Ray Lines observed during the Solar Activity of August 2 to August 11, 1972. *Nature* **241**, 333–335 (1973).
42. Chupp, E. L., Forrest, D. J. & Suri, A. N. High Energy Gamma-Ray Radiation above 300 KeV Associated with Solar Activity. In Kane, S. R. (ed.) *Solar Gamma-, X-, and EUV Radiation*, vol. 68, 341 (1975).
43. Chambon, G. et al. A hard X-ray and gamma ray observation of the 22 November 1977 solar flare. In NASA. Goddard Space Flight Center Gamma Ray Spectry. in *Astrophys.* p 70-75 (SEE N78-31971 22-88) (1978).
44. Summa, A., Elsässer, D. & Mannheim, K. Nuclear de-excitation line spectrum of Cassiopeia A. *Astron. Astrophys.* **533**, A13 (2011).
45. Weinberger, C., Diehl, R., Pleintinger, M. M. M., Siegert, T. & Greiner, J. ^{44}Ti ejecta in young supernova remnants. *Astron. Astrophys.* **638**, A83 (2020).
46. Liu, B., Yang, R.-z. & Aharonian, F. Nuclear de-excitation lines as a probe of low-energy cosmic rays. *Astron. Astrophys.* **646**, A149 (2021).
47. Liu, B., Yang, R.-z., He, X.-y. & Aharonian, F. New estimation of the nuclear de-excitation line emission from the supernova remnant Cassiopeia A. *Mon. Not. R. Astron. Soc.* **524**, 5248–5253 (2023).
48. Wei, Y.-J. et al. A Novel Model for the MeV Emission Line in GRB 221009A. *Astrophys. J. Lett.* **968**, L5 (2024).
49. Goldstein, A., Cleveland, W. H. & Kocevski, D. Fermi gbm data tools: v1.1.0 (2021). <https://fermi.gsfc.nasa.gov/ssc/data/analysis/gbm>.
50. Vianello, G. et al. The Multi-Mission Maximum Likelihood framework (3ML). *arXiv e-prints arXiv:1507.08343* (2015).
51. Lu, R.-J. et al. A Comprehensive Analysis of Fermi Gamma-Ray Burst Data. II. E_p Evolution Patterns and Implications for the Observed Spectrum-Luminosity Relations. *Astrophys. J.* **756**, 112 (2012).
52. Akaike, H. A new look at the statistical model identification. *IEEE Trans. Autom. control* **19**, 716–723 (1974).
53. Burnham, K. P. & Anderson, D. R. Multimodel inference: understanding aic and bic in model selection. *Sociological methods Res.* **33**, 261–304 (2004).
54. Freeman, P. E. et al. Resonant Cyclotron Radiation Transfer Model Fits to Spectra from Gamma-Ray Burst GRB 870303. *Astrophys. J.* **524**, 772–793 (1999).
55. Protassov, R., van Dyk, D. A., Connors, A., Kashyap, V. L. & Siemiginowska, A. Statistics, Handle with Care: Detecting Multiple Model Components with the Likelihood Ratio Test. *Astrophys. J.* **571**, 545–559 (2002).
56. Jeffreys, H. *The theory of probability* (OUP Oxford, 1998).
57. Thrane, E. & Talbot, C. An introduction to Bayesian inference in gravitational-wave astronomy: Parameter estimation, model selection, and hierarchical models. *PASA* **36**, e010 (2019).
58. Arnaud, K. A. XSPEC: The First Ten Years. In Jacoby, G. H. & Barnes, J. (eds.) *Astronomical Data Analysis Software and Systems V*, vol. 101 of *Astronomical Society of the Pacific Conference Series*, 17 (1996).
59. Gross, E. & Vitells, O. Trial factors for the look elsewhere effect in high energy physics. *Eur. Phys. J. C.* **70**, 525–530 (2010).

60. Bringmann, T., Huang, X., Ibarra, A., Vogl, S. & Weniger, C. Fermi LAT Search for Internal Bremsstrahlung Signatures from Dark Matter Annihilation. *JCAP* **07**, 054 (2012).
61. Weniger, C. A tentative gamma-ray line from Dark Matter annihilation at the Fermi Large Area Telescope. *J. Cosmol. Astropart. Phys.* **2012**, 007 (2012).
62. Ackermann, M. et al. Fermi-LAT Observations of the Gamma-Ray Burst GRB 130427A. *Science* **343**, 42–47 (2014).
63. Dalesi, S. Fermi GBM Team. GRB 230307A: Bad Time Intervals for Fermi GBM data. *GRB Coord. Netw.* **33551**, 1 (2023).

Acknowledgements

We acknowledge the use of the Fermi-GBM data provided by the Fermi Science Support Center. We thank Zi-Qing Xia, Xiaoyuan Huang, Rui-zhi Yang, Tian-Ci Zheng, Qiao Li, and Chang-Xue Chen for technical support. We also thank Rui-zhi Yang for theoretical insights. This work was supported by the Strategic Priority Research Program of the Chinese Academy of Sciences (grant No. XDB0550400), the National Key R&D Program of China (2024YFA1611704), the NSFC (No. 12473049, 12233011, 11921003, 12321003, 12225305). X.L is supported by the Youth Innovation Promotion Association CAS. H.N.He is supported by Project for Young Scientists in Basic Research of Chinese Academy of Sciences (No. YSBR-061), and by NSFC under the grants No. 12173091, and No. 12333006. Y.W is supported by the Jiangsu Funding Program for Excellent Postdoctoral Talent (grant No. 2024ZB110), the Postdoctoral Fellowship Program (grant No. GZC20241916) and the General Fund (grant No. 2024M763531) of the China Postdoctoral Science Foundation. J.R is support by the General Fund (grant No. 2024M763530) of the China Postdoctoral Science Foundation. Z.Q.S is supported by the NSFC (No. 12003074).

Author contributions

D.M.W and L.Y.J launched the project. L.Y.J, Y.W, X.L and Z.Q.S processed and analyzed the data. H.N.H, D.M.W, L.Y.J, J.R, Y.J.W and Z.P.J contributed to the theoretical interpretations to the event. All authors prepared the paper and joined the discussion.

Competing interests

The authors declare no competing interests.

Additional information

Supplementary information The online version contains supplementary material available at <https://doi.org/10.1038/s41467-025-57791-w>.

Correspondence and requests for materials should be addressed to Da-Ming Wei.

Peer review information *Nature Communications* thanks the anonymous reviewers for their contribution to the peer review of this work. A peer review file is available.

Reprints and permissions information is available at <http://www.nature.com/reprints>

Publisher's note Springer Nature remains neutral with regard to jurisdictional claims in published maps and institutional affiliations.

Open Access This article is licensed under a Creative Commons Attribution-NonCommercial-NoDerivatives 4.0 International License, which permits any non-commercial use, sharing, distribution and reproduction in any medium or format, as long as you give appropriate credit to the original author(s) and the source, provide a link to the Creative Commons licence, and indicate if you modified the licensed material. You do not have permission under this licence to share adapted material derived from this article or parts of it. The images or other third party material in this article are included in the article's Creative Commons licence, unless indicated otherwise in a credit line to the material. If material is not included in the article's Creative Commons licence and your intended use is not permitted by statutory regulation or exceeds the permitted use, you will need to obtain permission directly from the copyright holder. To view a copy of this licence, visit <http://creativecommons.org/licenses/by-nc-nd/4.0/>.

© The Author(s) 2025